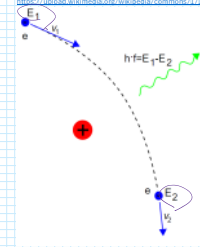


in
in permission

hydrated @Mond
kT

2. Explain the mechanisms of the continuum emission from thin-thermal plasmas



Thermal bremsstrahlung

3. If the hot plasma is only composed of hydrogen (protons and electrons), what kind of spectra are expected from thin-thermal plasma?

4. Indicate a simple approximate formula of the thermal bremsstrahlung spectrum.

5. Indicate examples of X-ray energy spectra from thin-thermal plasmas with different temperatures (say, from $kT=1$ keV to 20 keV). Observe changes of the energy spectra with temperatures paying attention to the following points:
 a. Emission lines
 b. Slope of the continuum in 1 - 10 keV
 c. Peak energy of the continuum

Figure 7: Left: XSPEC simulated spectrum (black) of the core of M87 as observed with 100 ks and the best-fitting model (red). Adapted from... Right: Plasma spectra from the core of the Perseus cluster. Broad-band spectrum is shown on the top panel (note that the gas cube was in place during the observation and it shows most X-rays below ~ 2 keV), while the second to the high-energy end spectrum is shown in the bottom panel. The best-fitting model is shown in red. Emission resolved individual lines in the spectrum (black vs. blue points).

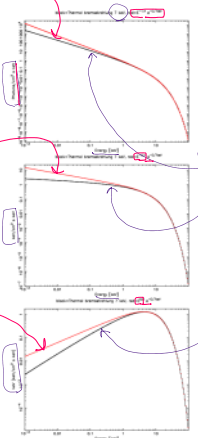


Figure 5.3: Comparison of $kT=7$ keV thermal bremsstrahlung spectra (black, brown model in xspec) and a cut-off power-law model $\propto (E/E_0)^{-\Gamma} \exp(-E/E_0)$ where $kT=7$ keV (red). From top to bottom, unit of the y-axis is $[10^{-14} \text{W/m}^2/\text{keV}/\text{cm}^2]$, $[\text{keV}^2/\text{keV}/\text{cm}^2]$ and $[\text{keV}^2/\text{s}/\text{keV}/\text{cm}^2]$, and the χ value is 1.4, 0.4, 0.6, respectively.

https://www.itatb.it/it/Room/ebisawa/ebisawa/TEACHING/2016/notes.pdf

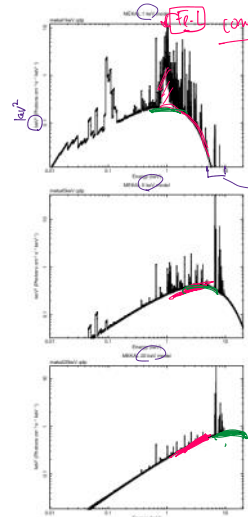


Figure 5.5: Theoretical energy spectra from thermal plasmas at 1 keV, 5 keV and 10 keV. The "mekal" model in XSPEC is used. We can see that, as the temperature increases, continuum peaks shift toward higher energies, and (2) emission lines from heavier are more prominent.

3. Thermal Comptonization

- Observed how the "cut-off power-law" spectra are formed by thermal (inverse) Comptonization process
- Observe how the spectral shape changes with the scattering optical depth
- In which objects the thermal comptonization spectra are expected?

$$y = \frac{4kT_e}{m_e c^2} \ln \tau \approx \frac{4kT_e}{m_e c^2} \tau$$

Thermal comptonization model

https://www.aanda.org/article/2015/01/01/1500158-007-0005-1.pdf

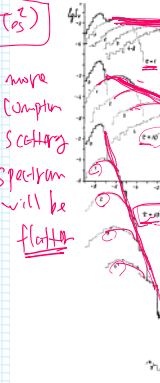


Figure 20: Comparison of low-frequency spectra in a cloud of weakly relativistic electrons for different values of the optical depth. Dashed curves represent the combination of the optical scattering cross-section and the electron scattering cross-section to form a power-law spectrum for the hard tail.

Longair, "High Energy Astrophysics"

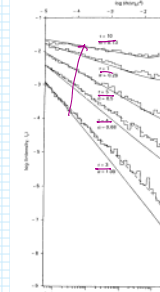


Figure 11: The Comptonization of low-frequency photons in a spherical plasma. The plot shows flux density vs. frequency for different optical depths.

1. Emission
 2. Absorption
 3. Scattering

Plasma is Hydrogen
 I Temperature is defined

BHB in lower hard state
 AGN

https://link.springer.com/content/pdf/10.1007/978-0-07-0005-1.pdf

A widely accepted model for Galactic black hole binaries

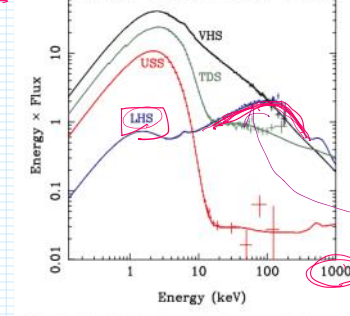


Fig. 9 The left hand panel shows a selection of states taken from the 2005 outburst of... The right hand panel shows the proposed accretion flow changes to explain these different differing contributions from the disc, hot inner flow and its associated jet, active regions above a wind

AGN accretion geometries under debate
 Andrzej A. Zdziarski, Barbara De Marco
 Sombreros and lampposts: The geometry of accretion onto black holes

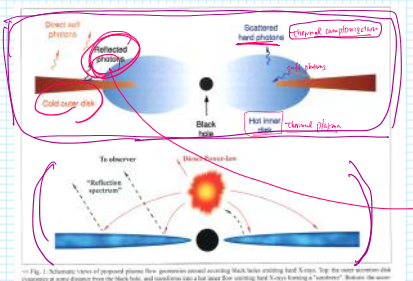


Fig. 1. Schematic view of proposed plasma flow geometry around accreting black holes emitting hard X-rays. The inner accretion disc comprises a zone (closer from the black hole), and lampposts (also that emit hard X-rays) emitting "Sombreros". Beyond the inner disc (the innermost white shell) around the black hole, the hard X-ray source of a "lamppost" type is located above the black hole.

Miyakawa, Ebisawa and Inoue (2012), PASJ, 64, 140

Partial Covering Model of MCG-6-30-15



https://ui.adsabs.harvard.edu/abs/2012MNRAS...421...140M

Thermal comptonization

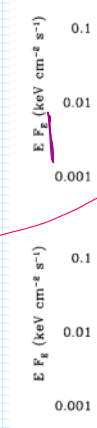
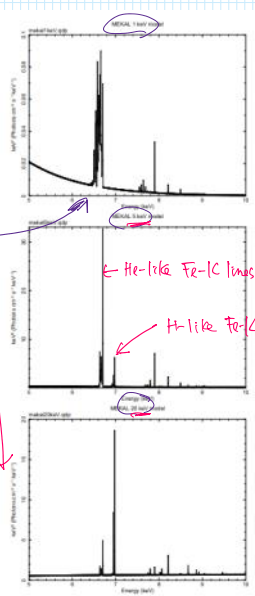


Figure 3

!!

lines from more highly ionized Fe ions
 Fe XXVI lines
 Fe XXV lines
 Fe XXIV lines
 Fe XXIII lines
 Fe XXII lines
 Fe XX lines
 Fe XIX lines
 Fe XVIII lines
 Fe XVII lines
 Fe XVI lines
 Fe XV lines
 Fe XIV lines
 Fe XIII lines
 Fe XII lines
 Fe XI lines
 Fe X lines
 Fe IX lines
 Fe VIII lines
 Fe VII lines
 Fe VI lines
 Fe V lines
 Fe IV lines
 Fe III lines
 Fe II lines
 Fe I lines

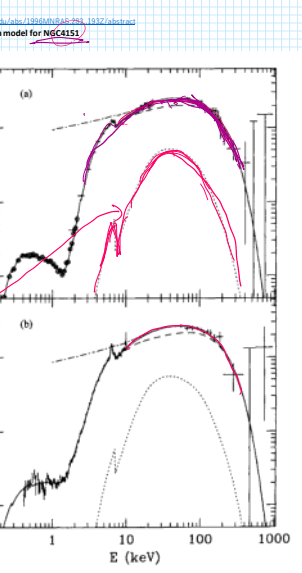


He-like Fe-K lines @ 6.67 keV
 H-like Fe-K line @ 6.97 keV

Figure 5.6: Expansion of the iron K-line region in the previous figure. Iron line missions from the 1 keV, 5 keV and 20 keV thermal plasmas are indicated. Around 6.6 - 6.7 keV, FeXXV (He-like) lines are seen, and around 7.0 keV, FeXXVI (H-like) lines are observed. As the plasma temperature increases, lines from more highly ionized ions are observed.

ultrasoft
 thermal dominant
 very high
 low/hard

GRO J1655-40.
 nt spectra, with
 ve the disc and



d_s photos $L_S / (4\pi d_s^2)$
 $d_s \sqrt{E}$

4. Non-thermal emission

Often non-thermal particle acceleration takes place in the universe (shocks, magnetic acceleration etc.), and each relativistic electron ($v \sim c$) has the energy $E = mc^2 \gamma$, where $\gamma = 1/\sqrt{1 - v^2/c^2} \gg 1$

The electron energy distribution $N(E)$ often becomes a power-law, as

$N(E)dE \propto \gamma^{-p} d\gamma$

non-thermal plasma

In the case synchrotron emission or relativistic inverse-Compton scattering, typical photon frequency ν , from a single electron with the energy $E = mc^2 \gamma$ is known to be proportional to γ^2 .

By integrating over the electron distribution, synchrotron spectra or relativistic inverse-Compton spectra may be expressed as

$F(\nu) \propto \int S(\nu/\nu_c) \gamma^{-p} d\gamma$

1. indicate the synchrotron emission or relativistic inverse-Compton scattering spectra become power law

$\propto \nu^{-s}$

$s = \frac{p-1}{2}$

$p=2 \Rightarrow s = \frac{2-1}{2} = 0.5$

3. Which sources are expected to emit non-thermal comptonization and/or synchrotron emission?

- Pulsars
- SXR (in shell)
- BBB (hard tail)

3. When the relativistic electrons, soft input photons (energy density U_{ph}) and magnetic field (energy density U_B) coexist, both the synchrotron emission and inverse-Comptonization take place simultaneously.

In the case of the SNR RX J1713.7-3946, observe that the following relationship holds between the synchrotron luminosity (P_{syn}) and the inverse-Comptonization luminosity (P_{IC}).

$\frac{P_{syn}}{P_{IC}} = \frac{U_B}{U_{ph}}$

see text book!

$B \approx 3 \mu G \Rightarrow v_B = 0.2 \text{ c}$

$U_{ph} \approx 0.3 \text{ eV/cm}^3$

4. In Fig. 19 of Aharonian et al. 2006, the relativistic electron energy distribution has been assumed to be $\gamma^p \exp(-m\gamma/E_0)$, where p is 2 and $E_0 = 100 \text{ TeV}$.

- (a) Inverse Compton spectral peak energy
- (b) Cut-off energy of the synchrotron spectrum and the inverse Compton spectrum
- (c) Slope of the synchrotron spectrum and the inverse Compton spectrum below the cut-off energies

$F(E) = \frac{E^{-0.5}}{(\text{erg/s/cm}^2/\text{keV})}$

$E F(E) \propto E^{-0.5}$

$(\text{erg}^2/\text{s/cm}^2/\text{keV})$

(erg/s/cm^2)

Synchrotron and Inverse Compton model for the supernova remnant RXJ1713.7-3946

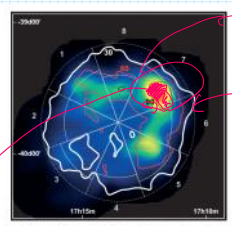


Fig. 15. ASCA X-ray (1-5 keV band, Uchiyama 2005) image of RX J1713.7-3946, overlaid with contours of the smoothed, acceptance-corrected HESS gamma-ray image. The colored contour levels are labeled and linearly spaced at 30, 60, and 90 counts. Drawn as gray thin lines are eight wedge-shaped regions for which the radial profiles are compared to each other in Fig. 16. Note that in the ASCA image, most of the regions (thin solid lines) do not reach as far as in the HESS image (thin dashed lines), accelerating for the limited field of view of ASCA, whose coverage did not always extend to the boundaries of the SNR. As explained in the main text, the ASCA image was stretched to match the HESS point spread function to enable comparison of the two images.

ASCA image $(1-5 \text{ keV})$

HESS TeV

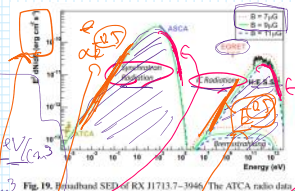


Fig. 19. Broadband SED of SNR RX J1713.7-3946. The ATCA radio data and ASCA X-ray data (Hiraga 2005) for the whole SNR are indicated, along with the HESS measurement and the Fermi-LAT upper limit. Note that the radio flux was determined to be $1.5 \pm 0.05 \text{ mJy}$ for the western part of the shell and was scaled up by a factor of two here to account for the whole SNR. The synchrotron and IC spectra were modeled assuming a source distance of 1 kpc, an age of 1000 years, a density of 1 cm^{-3} , and a production rate of relativistic electrons by the acceleration mechanism in the form of a power law of index $\alpha = 2$ and an exponential cutoff of $E_0 = 100 \text{ TeV}$. Shown are three curves for three values of the mean magnetic field: 7 μG , 9 μG , and 11 μG , to demonstrate the required range of the B field strength for this scenario. The electron luminosity is adopted such that the observed X-ray flux level is well matched. For the three magnetic field values the luminosity L_e is $L_e = 1.77 \times 10^{37} \text{ erg s}^{-1}$ (7 μG), $L_e = 1.14 \times 10^{37} \text{ erg s}^{-1}$ (9 μG), and $L_e = 0.81 \times 10^{37} \text{ erg s}^{-1}$ (11 μG).

THE ASTROPHYSICAL JOURNAL, 773:138 (2013) August 20

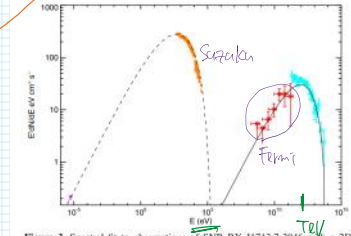


Figure 3. Spectral fit to observations of SNR RX J1713.7-3946 with a 2D MHD simulation. The different emission processes are synchrotron (dashed line), IC (solid line). The data are from Acero et al. (2009); in radio, Tanaka et al. (2006); Suzaku X-ray, Ablo et al. (2011); Fermi-LAT, and Aharonian et al. (2006; HESS). Note that the two lowest energy Fermi-LAT points are upper limits. The seed photon field in the IC process includes an IR component with a temperature of $T = 30 \text{ K}$ and an energy density of 1.2 eV cm^{-3} and the microwave background radiation (Li et al. 2011).

Partial Covering Model of MCG-6-30-15

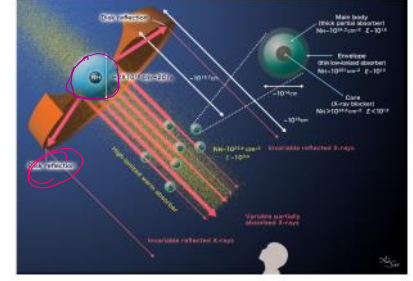
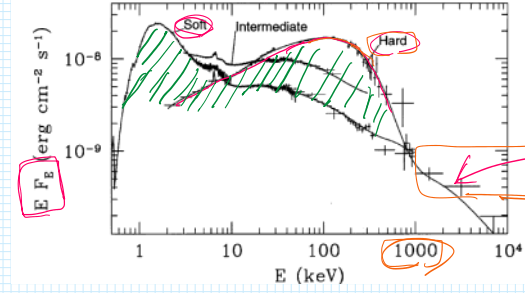


Fig. 12. Schematic picture of the variable partial covering model for MCG-6-30-15 and the internal structure of the absorbing cloud.

Thermal compton & non-thermal compton model for Cyg X-1



$E F_s (\text{erg cm}^{-2} \text{s}^{-1})$

hard tail

$k_e \propto \gamma^2$

Synchrotron
inverse Compton
relativistic

$F(\nu) = \int S(\nu/\nu_c) \dots$

$= \int S(\nu/\nu_c) \dots$

Synchrotron and inverse-Compton model for Crab pulsar

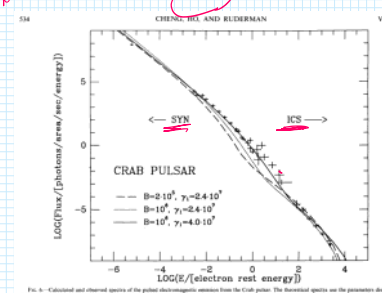


Fig. 4. Calculated and observed spectra of the pulsed electromagnetic emission from the Crab pulsar. The theoretical spectra are the parameters described in Table 1. The observed data are from 1970-1990. The dashed and solid lines represent the synchrotron and inverse-Compton emission, respectively. The dotted line shows the total emission. The solid line shows the total emission with the synchrotron emission subtracted. The observed data are from Aharonian et al. (2006) and the Crab pulsar emission from the Crab pulsar. The data are from Aharonian et al. (2006) and the Crab pulsar emission from the Crab pulsar.

$mc^2 \gamma = 100 \text{ TeV}$

$\gamma = \frac{100 \text{ TeV}}{511 \text{ keV}} = \frac{10^2 \cdot 10^6}{5 \cdot 10^2 \cdot 10^3} = \frac{10}{5} \cdot \frac{10^3}{10^3} = 2 \cdot 10^8$

CMRB 2.7 K

BB $T_{\text{peak}} \approx 2.8 T_{\text{BB}}$

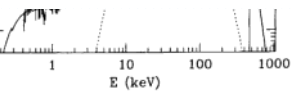
$\approx 2.8 \cdot 2.7 \approx 8 \text{ K}$

$\approx 7 \cdot 10^4 \text{ [eV]}$

$1 \text{ eV} \approx 11604 \text{ K}$

$7 \times 10^4 \times (2 \cdot 10^8)^2 \approx 7 \times 10^4 \times 4 \cdot 10^{16} = 28 \times 10^{20} \text{ [eV]}$

$\approx 30 \text{ TeV !!}$



X-ray spectra of NGC 4151 as observed (a) in 1991 by *ROSAT*, *Ginga* and OSSE, and (b) in 1993 May by OSSE. The dashed curves give the absorbed thermal emission spectra, the dotted curves give the reflection component, the solid curves give the models of the observed spectra, the dot-dashed curves give the unabsorbed continua (soft X-ray excess and the K α line). The model parameters are given in Table 1. The plotted data have been rebinned for the upper limits are 2σ . The *ROSAT* data are marked with open circles. The data from all four *ASCA* detectors have been co-added.

Derive

$$= \frac{p-1}{2} \int N(E) \propto \gamma^{-p} d\gamma$$

$$\nu^2 \int S(\nu/\nu_c) \gamma^{-p} d\gamma$$

Single electron spectrum
 $E = mc^2 \gamma$

emission
Compton scattering
typical photon energy
 ν_c (frequency)

$$\rightarrow \frac{d\nu}{\nu} \propto \frac{d\gamma}{\gamma} \propto \nu_c \cdot d\left(\frac{1}{\nu}\right)$$

$$\gamma^{p+1} \frac{d\gamma}{\gamma} \propto \frac{\nu_c}{\nu} \cdot d\left(\frac{1}{\nu}\right) = \left(\frac{\nu_c}{\nu}\right)^{-1} d\left(\frac{1}{\nu}\right)$$

$$\propto \nu_c^{-\frac{p+1}{2}} \cdot \left(\frac{\nu_c}{\nu}\right)^{-1} d\left(\frac{1}{\nu}\right)$$

$$= \int S(\nu/\nu_c) \cdot \left(\frac{\nu_c}{\nu}\right)^{-\frac{p+1}{2}} \cdot \left(\frac{\nu_c}{\nu}\right)^{-1} \cdot \left(\frac{\nu_c}{\nu}\right)^{-1} d\left(\frac{\nu_c}{\nu}\right)$$

$$= \nu_c^{-\frac{p+1}{2}} \int S(\nu/\nu_c) \cdot \left(\frac{\nu_c}{\nu}\right)^{-\frac{p-3}{2}} d\left(\frac{\nu_c}{\nu}\right)$$

$$\propto \nu_c^{-\frac{p-1}{2}} \rightarrow \text{const.}$$